AIP The Journal of Chemical Physics

Pressure dependence of confined liquid behavior subjected to boundary-driven shear

D. M. Heyes, E. R. Smith, D. Dini, H. A. Spikes, and T. A. Zaki

Citation: J. Chem. Phys. **136**, 134705 (2012); doi: 10.1063/1.3698601
View online: http://dx.doi.org/10.1063/1.3698601
View Table of Contents: http://jcp.aip.org/resource/1/JCPSA6/v136/i13
Published by the American Institute of Physics.

THE JOURNAL OF CHEMICAL PHYSICS **136**, 134705 (2012)

Pressure dependence of confined liquid behavior subjected to boundary-driven shear

D. M. Heyes,[a] E. R. Smith,[b] D. Dini,[c] H. A. Spikes,[d] and T. A. Zaki[e]

Department of Mechanical Engineering, Imperial College London, Exhibition Road, South Kensington, London SW7 2AZ. United Kingdom

(Received 25 January 2012; accepted 13 March 2012; published online 4 April 2012)

Non-equilibrium molecular dynamics simulations of boundary-driven sheared Lennard-Jones liquids at variable pressure up to 5 GPa (for argon) reveal a rich out-of-equilibrium phase behavior with a strong degree of shear localization. At the lowest apparent shear rate considered (wall speed $\sim$1 m s^{-1}) the confined region is an homogeneously sheared solid (S) with no slip at the walls. This transforms at higher shear rates to a non-flowing plug with slip at the walls, referred to as the plug slip (PS) state. At higher shear rate a central localized (CL) state formed in which the shear gradient was localized in the center of the film, with the rest of the confined sample in a crystalline state commensurate with the wall lattice. The central zone liquidlike region increased in width with shear rate. A continuous rounded temperature profile across the whole system reflects strong dynamical coupling between the wall and confined region. The temperature rise in the confined film is consistent with the Brinkman number. The transition from the PS to CL states typically occurred at a wall speed near where the shear stress approached a critical value of $\sim$3% of the shear modulus, and also near the peak in the traction coefficient, μ. The peak traction coefficient values computed, $\sim 0.12 - 0.14$ at 1000 MPa agree with those found for traction fluids and occur when the confined liquid is in the PS and CL states. At low wall speeds slip can occur at one wall and stick at the other. Poorly wetting liquids manifest long-lived asymmetries in the confined liquid properties across the system, and a shift in solid-liquid phase co-existence to higher shear rates. A non-equilibrium phase diagram based on these results is proposed. The good agreement of the tribological response of the Lennard-Jones fluid with that of more complicated molecular systems suggests that a corresponding states scaling of the tribological behavior could apply. [http://dx.doi.org/10.1063/1.3698601]

I. INTRODUCTION

Over the last few decades there has been much interest in the behavior of confined and sheared molecularly thin liquid films, e.g., in the surface forces apparatus (SFA) and thin film lubrication applications. Evidence from experiment and molecular simulation[1] indicates that the confined liquid molecules can order into a semi-solid state at ambient pressures purely through the influence of the confining walls, which is reflected in anomalous tribological signatures such as so-called, "stick-slip" behavior in SFA. There is experimental evidence for the slip of small-molecule liquids near solid walls under continuous flow conditions.[2–4] Wall-liquid slip in nanoflows can be an advantage, e.g., by increasing pressure-driven flow rate, or a disadvantage, by reducing traction between the walls and mixing of components within the channel. Non-equilibrium molecular dynamics (NEMD) simulation has proved a useful theoretical tool for investigating this basic geometry, since the pioneering work of Ashurst and Hoover,[5] and later, for example, by Liem *et al.*[6] Advances in the statistical mechanical foundation of boundary-driven shear flow,[7] and applications of NEMD to ever more complex organic molecules,[8] make it an increasingly useful and accurate tool to complement tribological experiments. NEMD obviates the need to make assumptions about the rheological constitutive equation and fluid-solid boundary conditions of molecularly thin confined liquids under shear.

Boundary-driven NEMD simulation with thermostatted sliding walls is finding increasing popularity as a means of initiating and sustaining shear flow because it mimics closely a typical experimental arrangement. NEMD simulations have revealed a number of features of liquid flow in a nano-channel which are not predicted by and are beyond the capability of classical continuum hydrodynamic treatments. It has been found many times that several layers of molecules can be essentially immobilised ("epitaxially bound") next to the walls.[9] The form of the wall-liquid molecular interactions can be used to control the degree of layering and slip near the wall.[10] At low shear rate, the slip length appears to be a characteristic feature of these interactions, largely independent of the type of flow.[11] However, the slip length has been observed to both increase[12,13] and decrease,[14] with shear rate, if the liquid or walls are thermostatted, respectively (see further discussion of the origins of these differences in Refs. 14 and 15). Recent experiment and theoretical models provide evidence

---

[a] Electronic mail: d.heyes@imperial.ac.uk.
[b] Electronic mail: edward.smith05@imperial.ac.uk.
[c] Electronic mail: d.dini@imperial.ac.uk.
[d] Electronic mail: h.spikes@imperial.ac.uk.
[e] Electronic mail: t.zaki@imperial.ac.uk.

for a decrease in slip length with increasing shear rate.[16] The structure and level of epitaxial adhesion between the wall and adjacent liquid molecules has a strong influence on the microscale flow and velocity profile in that region.[9,17] Stick boundary conditions are more likely to occur when the liquid molecules can form layers which are commensurate with the boundary wall atoms.[18]

Shear-initiated phase changes in the confined sample have been studied experimentally and by molecular simulation. Transitions from solid to liquid have been observed, accompanied by shear rheological softening. Mokshin and Barrat,[19,20] reported the results of NEMD simulations of an initially glassy Lennard-Jones (LJ) assembly of particles sheared via amorphous boundaries into crystalline grains. There was localization of the shear velocity gradient in bands near the solid walls ("slip"), with the central region behaving like a "plug". Such shear localization or "banding" has also been observed in many systems under shear, for example, for foams,[21] granular materials,[22] liquid lubricants flowing at high pressure,[23] triblock copolymer micellar solutions,[24] colloidal liquids,[25] pastes,[26] and metallic glasses.[27] Why does this banding occur? The shear stress applied by a sliding boundaries experiment must be constant at steady state across the system for reasons of mechanical stability. The sample will flow or shear most where the yield stress or local viscosity is least, which can be at the walls or near the center of the channel depending on the structures formed in the channel. The flow characteristics are, therefore, intimately connected with the state of order and density variations in the channel. The strong variation of physical properties on a molecular scale in a molecularly thin channel has motivated the proposal of a non-local viscosity kernel.[28,29]

Bair *et al.*[30] observed shear localization in high pressure flow experiments of liquid lubricants under shear. The shear bands were inclined typically at ~20° to the walls and occurred just before the traction ("friction") coefficient became strongly nonlinear with shear rate. Time averaged velocity profiles showed no evidence of continuous slip at the walls or in the bulk, although localized slip of the bands was observed. The band formation was shown to be consistent with the Mohr-Coulomb failure criterion. A different type of shear localization due to a temperature rise and unstable temperature profile in the oil film was reported by Bair *et al.*[31] A thin hot layer became sandwiched between two cooler layers. The shearing was localized in the hot layer, and this transition was referred to as *adiabatic shear localization*. A possibly related phenomenon, of solid-liquid coexistence has been observed during homogeneous shear NEMD simulations.[32] Perhaps relevant to this experimental study, Butler and Harrowell using boundary-driven shear NEMD, established the nature of two coexisting layers in relative sliding motion, in their case between a crystal and liquid phase.[33,34] Tribology is one area where the NEMD shear rate and film thickness can agree with experiment.

Knowledge of the pressure, P, or normal load dependence of the non-equilibrium phase diagram could be relevant in guiding, for example, the design of lubricants and optimum conditions for elasto-hydrodynamic lubrication (EHL). For sliding-wall generated Couette flow in a nano-scaled channel, the independent variables of a non-equilibrium phase diagram include the intermolecular potentials between the various components ("global" or applied) shear rate, film thickness, and applied pressure. Measures of the streaming velocity profile and particle assembly ("phase") distribution between the walls are the dependent variables. NEMD simulations have shown that there is a transition from "equilibrium" or mainly T-controlled, to shear-controlled ("athermal") behavior above a critical shear rate.[35] Fluctuations in the particle velocities are increasingly driven by the shear itself as applied shear rate increases.

Elucidating additional aspects of this rather complex, multiparameter phase diagram is the purpose of the present work. The focus is to investigate by NEMD how applied pressure and global shear rate affect the behavior of the confined liquid sample. The molecular order, the velocity, density, and temperature profiles are examined as a function of the imposed system parameters. It is shown that the occurrence or lack of slip, an important consideration in experimental studies, is an integral characteristic of the phase diagram, being a natural response of any confined liquid under certain conditions. The emphasis here is in the steady state shear solutions for wall speeds in excess of ~1 m s^{-1}, which are more typical of tribological experiments of engineering interest than of surface force measurements, for example. The model adopted uses the Lennard-Jones potential which has the advantage that it to some extent can be considered to be scale-invariant and, therefore, is not tied to a particular lengthscale as would be the case for a model polyatomic molecule represented in terms of atom-atom potentials. The LJ system has been shown to capture the key physics of more complicated molecular systems under shearing non-equilibrium conditions,[36,37] and one might reasonably anticipate the same conclusion for the tribology.

II. SIMULATION METHOD

The NEMD model system consisted of a set of LJ molecules confined between two solid parallel LJ walls. The system was periodic in the x (streamwise) and z (spanwise) directions and bounded by walls in the y direction. The atoms in the system interacted via the LJ potential

$$\phi_{kl}(r) = 4\epsilon_{kl}\left[\left(\frac{\sigma}{r}\right)^{12} - c_{kl}\left(\frac{\sigma}{r}\right)^{6}\right], \qquad (1)$$

where the indices k and l refer to the types of atoms involved in the pair interaction, either confined phase (c) or solid wall (w). The potential parameters, σ and $\epsilon \equiv \epsilon_{cc}$, specifying the interaction range and energy of attraction, respectively, form the basis of the reduced system of units used here. The interactions were truncated at $r = 2.5\sigma$, and all atoms had the same mass, m. For the cross-interactions, the energy parameter was determined (as usual) from the geometric mean of the wall-wall and confined molecule self-values, $\epsilon_{ce} = (\epsilon_{ww}\epsilon_{cc})^{1/2}$. The reduced temperature used for all simulations was $T^* = k_B T/\epsilon = 1$, where k_B is Boltzmann's constant. A range of ϵ_{ww} values between 1 and 4 was investigated. The wetting parameter, c_{kl} was unity for ww and cc self-combinations, but ≤ 1 for the wc cross interactions. The confined fluid wets the wall less as

c_{wc} ($\equiv c$) becomes smaller. The value $c = 0.1$, for example, used here gives the non-wetting contact angle of ∼180°.[38] Using the LJ parameters for argon ($\epsilon/k_B = 120$ K and $\sigma = 0.340$ nm), the reduced units for pressure and speed are 42.1 MPa and 158 m s^{-1}, respectively. The solid wall reduced density was 1.063, which corresponds to 1.79 g cm^{-3}. The simulations were carried out for applied normal pressures up to 119 in LJ reduced units or equivalently 5000 MPa, which encompasses the usual elastohydrodynamic lubrication experimental range. Pressures in the range 1–5000 MPa were considered in the simulations.

The NEMD equations of motion of Petravic and Harrowell (PH) employing an anharmonic tethering potential to constrain the wall atoms to vibrate about the lattice sites were used.[7,39] Each confining wall was made up of 8 FCC (100) planes of atoms, some or all of which were thermostatted. The wall atoms evolved according to classical mechanics. The half-step leap-frog Verlet algorithm,[40] was used for the central region molecules, $\underline{\ddot{r}}_i = \underline{F}_i/m_i$, where these quantities are the acceleration, force and mass for molecule i, respectively. The time step used was 0.001–0.002 in LJ reduced units. The means by which a steady-state temperature profile can be achieved is a major issue for boundary-driven shear flow, as it has been shown to affect strongly the behavior and physical state of the confined liquid.[14,15,41,42] The wall atoms rather than the confined atoms were thermostatted here as, of all the possible methods, it causes the least interference with the confined atom dynamics and corresponds closest to the experimental situation. The central region molecules were not thermostatted, nor subjected to a directly imposed velocity profile.

The equations of motion of the wall atoms were as follows. The imposed sliding speed in the x-direction was $v_x > 0$ for the top wall, and $-v_x$ for the bottom wall. The instantaneous force on the walls per unit area, or average normal pressure, P_N, was constrained to fluctuate about a desired value, P^0, by the equations of motion given below.[43] A pressure-control damping parameter, Q_p, determined the time scale of the normal pressure fluctuations, which was set to, $Q_p = P^0$. The mean velocity of the upper wall was v_y and the lower wall was $-v_y$, where

$$v_y = (P_N - P^0)/Q_p. \tag{2}$$

On average at steady state, $<v_y> = 0$. For unthermostatted wall atoms

$$\begin{aligned} \underline{\dot{r}}_i &= \underline{p}_i/m \pm v_x u_x \pm v_y u_y, \\ \underline{\dot{p}}_i &= \underline{F}_i, \end{aligned} \tag{3}$$

where u_α is the unit vector component in the α cartesian direction, and $\underline{p}_i$ is the peculiar momentum of atom, i. For the thermostatted wall atoms, the Nosé-Hoover (NH) thermostat was one of the methods employed

$$\begin{aligned} \underline{\dot{r}}_i &= \underline{p}_i/m \pm v_x u_x \pm v_y u_y, \\ \underline{\dot{p}}_i &= \underline{F}_i - \alpha \underline{p}_i, \\ \dot{\alpha} &= (T - T_0)/Q_T, \end{aligned} \tag{4}$$

where α is the NH thermostatting parameter, T is the instantaneous temperature of the thermostatted wall atoms derived from the kinetic energy based on the peculiar momenta, T_0 is the desired temperature, and Q_T controls the time scale of the temperature fluctuations ($Q_T = 5$ in LJ time units was used). The two walls were thermostatted individually. For comparison, some of the simulations were conducted with the velocity scaling (VS) thermostat, applied to the wall atom peculiar momenta.[44]

The lower wall, confined atoms, and upper wall are referred to as regions A, B, and C, respectively, constructed out of a face-centered cubic (FCC) lattice. The number of basic FCC cubes of 4 atoms in the x, y, and z directions were 6 × 4 × 6, 6 × 10 × 6, and 6 × 4 × 6, for regions A, B, and C, respectively, for most of the simulations. There were 576 atoms in each wall and 1440 atoms in the confined region, giving a 2592 atom system. The sidelength, S_x in the streamwise and spanwise directions was 9.33. A larger system of 4032 atoms was also simulated, where there were 20 basic cubic cells in the y-direction in region B. The lattice spacing of the wall region was independent of applied pressure, which is a reasonable assumption for typical metallic or inorganic wall materials as the confined liquid is more compressible than the solid wall material. The equilibration and production simulations were usually for 30 − 100 and 200 ps, respectively, which are short compared to typical residence times of lubricants in EHL contacts (∼1 ms). Hence any NEMD states or phase changes observed here would have more time to develop in the corresponding experimental system. The global shear rates are less than ∼0.2 LJ reduced units, which although giving an almost Newtonian response for liquids at ambient pressure, can lead to highly non-Newtonian behavior at the high pressures considered here (as will be shown). The pressure in EHL lubrication contact might typically be 2–3 GPa, which is within the range of the load pressures considered in the present simulations. These simulations were carried out under steady state conditions, so specifically time-dependent effects such as "stick-slip," yield stress, aging, and rejuvenation,[45] effects were not considered. A range of wall parameters was used to test their impact on the computed behavior. A summary of the set of system input parameters is given in Table I. The trends reported here were found to be qualitatively insensitive to the wall parameters, and the set $S2$ of intermediate value wall parameters was used for most of the figures reported herein.

III. RESULTS AND DISCUSSION

Figure 1 shows snapshot structures of the molecule coordinates projected onto the xy plane from a sequence of NEMD simulations carried out at applied pressures in the range 1–4000 MPa. The wall speed was $v_x = 1$ m s^{-1} in each simulation. The pressure was first progressively increased (top row, left to right in the figure) and then decreased (bottom row, right to left). This approach was adopted to explore any hysteresis effects and, therefore, the reversibility of any features on the NEMD timescale. The S2 set of parameters listed in Table I was used in the simulations. The global shear rate γ_g ($= 2v_x/h$, where h is the thickness of the central region), is

TABLE I. Summary of simulation details. The production simulations were carried out for between 2850 reduced time units at $v_x = 2$ m s^{-1}, and 950 reduced time units at $v_x = 150$ m s^{-1}. Key: # is the simulation parameter set code. There were $N = 2592$ atoms in each model system. ϵ_{ww} is the Lennard-Jones potential parameter between the wall atoms. *NLT* is the number of tethered wall layers thermostatted. *Th* is the type of thermostat used in the simulation. *NH* denotes Nosé-Hoover and *VS*, the peculiar velocity scaling thermostats. *c* is the wall-slip potential parameter between wall and liquid atoms in Eq. (1). $v_{x,1}$ is the wall speed at which the transition from Plug Slip (PS) to central region shear localization (CL) takes place on ascending wall speed. $v_{x,2}$ is the wall speed where the PS-CL transition occurs during decreasing wall speed. Columns 6 and 7 are for a load pressure of 1000 MPa, and the last two columns are for 5000 MPa. The numbers in the brackets are the estimated uncertainties arising from the finite increments in the wall speed used in the NEMD run sequence.

#	ϵ_{ww}	*Th*	*NLT*	*c*	$v_{x,1}$ 1000 MPa	$v_{x,2}$ 1000	$v_{x,1}$ 5000 MPa	$v_{x,2}$ 5000
S1	4	NH	2	1.0	30(10)	30(10)	100(10)	70(10)
S2	2	NH	2	1.0	30(10)	30(10)	70(10)	55(5)
S3	1	NH	2	1.0	15(5)	15(5)	30(10)	30(10)
S4	2	NH	8	1.0	30(10)	30(10)	125(25)	80(10)
S5	2	NH	2	0.1	70(10)	40(5)	70(10)	60(10)
S6	2	VS	8	1.0	30(10)	30(10)	90(10)	70(10)
S7	2	VS	2	1.0	20(5)	30(10)	60(5)	50(5)

rather small by NEMD standards (~0.001 in reduced units), at least for liquids at ambient pressure. The dimension of the central region decreased by about a half in the *y*-direction going from a pressure of 1 to 4000 MPa. Up to pressures between 100 and 200 MPa, the figure reveals that the confined molecules adopted a liquidlike arrangement with some layering next to the wall (frame 1, top left). With increasing pressure the confined atoms ordered progressively from the wall inwards (frames 2–4 in the top row), and at a pressure of 500 MPa (frame 5) they had formed a strained single crystal. On decreasing *P* this sequence of structures was repeated to a large extent at the same wall speeds, but with some hysteresis; for example, compare the two 100 MPa frames in Fig. 1. The semicrystalline confined material evolved under strain through a sequence of lattice dislocations, apparent in Fig. 2. The frames on the top row of Fig. 2 are from the $P = 500$ MPa and $v_x = 1$ m s^{-1} simulation of Fig. 1. The views are with the *xy* and *zy* boundary edge face-on in the middle with *y* vertical. This figure demonstrates that dislocation events accommodate the global straining, while the crystalline order is retained on average.

Figure 3 shows the *xy* plane coordinate projections at wall speeds in the range $2 - 150$ m s^{-1} at a constant applied

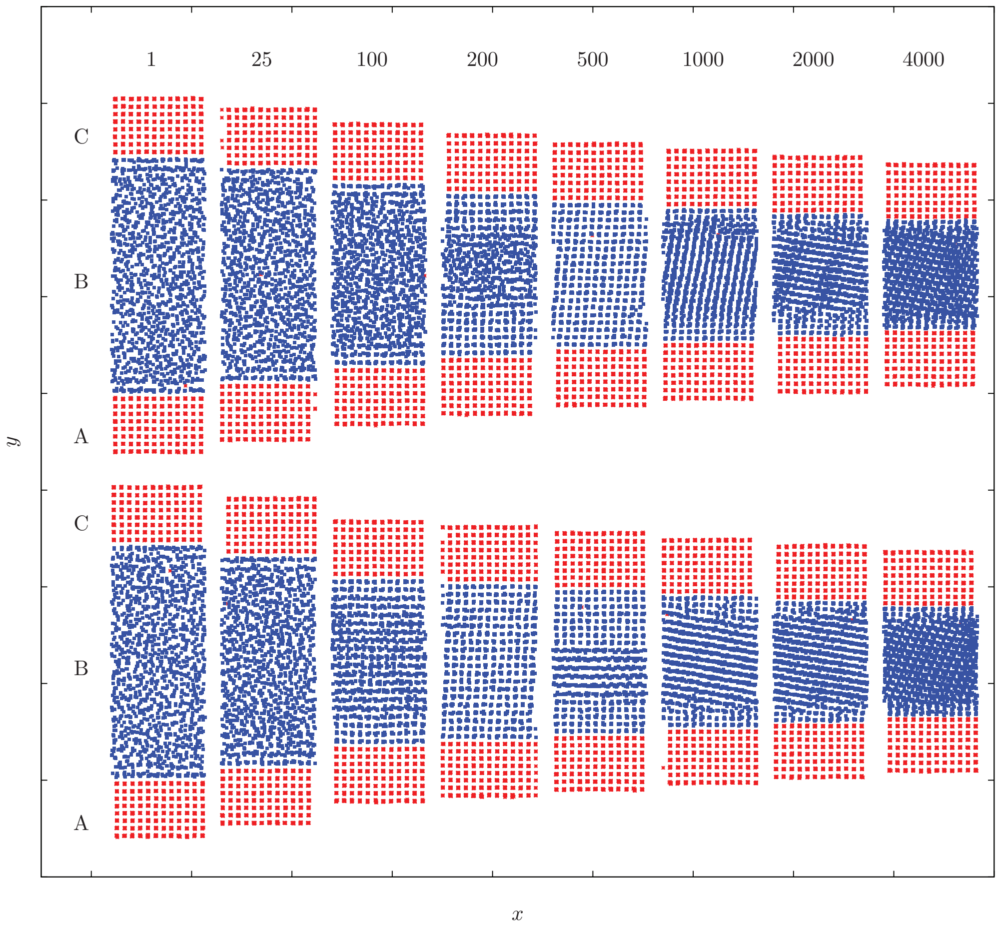

FIG. 1. Projections of the instantaneous particle coordinates on the *xy* plane. The distance increments in the *x* and *y* directions are 10σ. The wall speed was 1 m s^{-1}, and the applied pressures used are given in MPa above the top row. The simulation parameter set *S*2 specified in Table I was used. There were $N = 2592$ atoms in the system. Ascending pressure is from left to right along the top row, and decreasing pressure is right to left along the bottom row. The solid tethered wall atoms are red online and confined atoms are blue online.

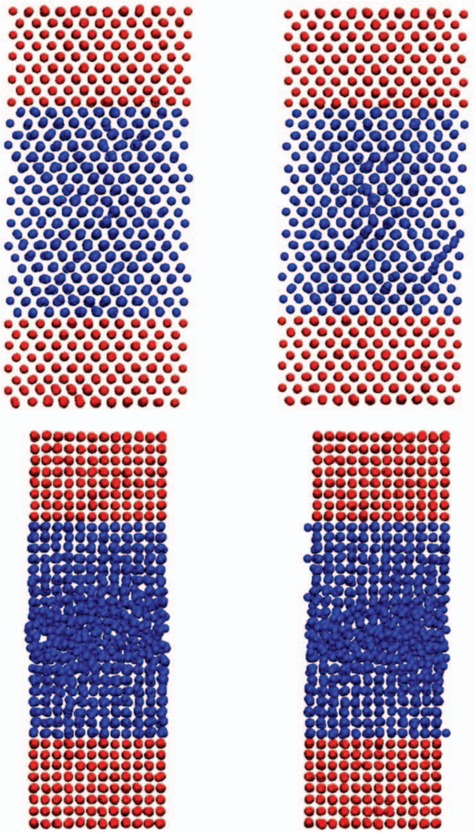

FIG. 2. Frames on the top from a NEMD simulation with (top two frames) $P = 500$ MPa and $v_x = 1$ m s^{-1} from Fig. 1. Two snapshots at different times are shown, viewed with the xy and zy boundary edge face-on in the middle with y vertical, and along the bottom, for $P = 1000$ MPa and $v_x = 50$ m s^{-1}. The views for the lower two frames is the xy. The images were plane, with y vertical made with the VMD graphics package.[72]

pressure of 1000 MPa using the S2 parameter set. The equilibrium LJ phase diagram indicates that the confined atoms should be in the solid state at this temperature and pressure.[46] With increasing global shear rate, the large crystallite in the center increasingly orients parallel with the wall, and there is a transition to significant solid-wall registry at a wall speed of 30 ± 10 m s^{-1}. Only the central part of region B looks disordered. This restructuring is designated the *central localization* (CL) phase. The thickness of the disordered central region is seen to increase with shear rate. Butler and Harrowell,[33] also showed by boundary-driven shear flow NEMD that there is a stationary coexistence between a strained crystal and a sheared liquid, with the liquid fraction proportion increasing with shear rate. The CL phase is in fact seen in Fig. 1 in the top row 200 MPa frame, but is apparently only stable over a narrow pressure range at $v_x = 1$ m s^{-1}. Figure 2 gives a more detailed picture of the dynamical evolution of the $P = 1000$ MPa and $v_x = 50$ m s^{-1} CL state. Two xy plane snapshots at different times are presented, with y vertical. They show that the internal dynamics and microstructure of the disordered central region and more solidlike zones near the walls are dynamically strongly coupled. The volume of these two regions fluctuates with time, and there are many dislocations in the solid region. Between wall speeds of 20 and 40 m s^{-1}, the time average density profile, $\rho(y)$, of the central region of atoms shows pronounced oscillations extending from the walls to the center, reflecting enhanced layering associated with the CL phase. At a wall speed of 150 m s^{-1}, the layering has disappeared (except $3 - 4$ layers next to the walls) and there is a uniform density distribution in the central part of the confined film, which is consistent with adiabatic shear of Bair *et al.* localized liquid state.[31]

Figure 4 presents the x-velocity profiles for the central region and wall atoms for the $P = 1000$ MPa states using the S2 set of parameters. Fluctuations in the confined molecule velocity are greatest near the wall, as might be expected because of the stiffer dynamics of the wall atoms. The apparent magnitude of these fluctuations is magnified for the low sliding speeds as the molecule velocities are normalized by the wall speed (which can be much smaller than the root mean square velocity at the target temperature in this limit). The figure shows shear localization ("slip") near the wall for speeds up to ∼20 m s^{-1}, with the middle part of the confined region acting as a "plug" with no noticeable internal shear flow. The figure demonstrates that at low wall speeds slip can occur at both walls or just one (with the confined molecules "sticking" to the other wall). This "plug slip" or *PS* state has also been observed in experiment, for example, during flow in concentrated colloidal suspensions,[47] and simulations of wall-driven shear of model granular systems.[48] The sheared region velocity profile near the walls is almost linear, and the boundary between the sheared (low viscosity) and unsheared (high viscosity) regions occurs within a narrow distance range of just several particle diameters. At $v_x = 40$ m s^{-1} the CL nonequilibrium state is evident. It is reasonable to assume that the PS-CL transformation is promoted by the steady increase in shear stress in the gap with increasing wall speed (further discussed below). With increasing global shear rate (hence shear stress) the plug region became increasingly more strained through elastic deformation. Once the yield stress of the plug had been exceeded, domain *B* exhibited shear localization preferentially in the center of the gap, as near the walls the confined atoms were able to form a more energetically favorable state of assembly and acquire additional shear mechanical strength by being in registry with the tethered wall atoms. Figure 4 shows that during descending wall speed, the shear band thickness evolution with wall speed is reproduced quite well. It is still an open question what determines the thickness of the liquidlike bands above the CL transition. Butler and Harrowell provide evidence that at steady state the relative amounts of the two phases is the result of a competition between crystal growth rate and surface erosion of the crystal.[33]

Figure 5 presents the temperature profiles across the system in the y-direction for the simulations of Fig. 4. The local temperature was derived from the x, y, and z components of the peculiar momenta kinetic energy, which show no statistical difference. At all wall speeds the temperature profile is nearly parabolic, as would be expected for Couette flow. The temperature in each case had its maximum in the center of the gap, which increased with wall speed. It is possible that the progressive rise in confined region average temperature with shear rate is responsible

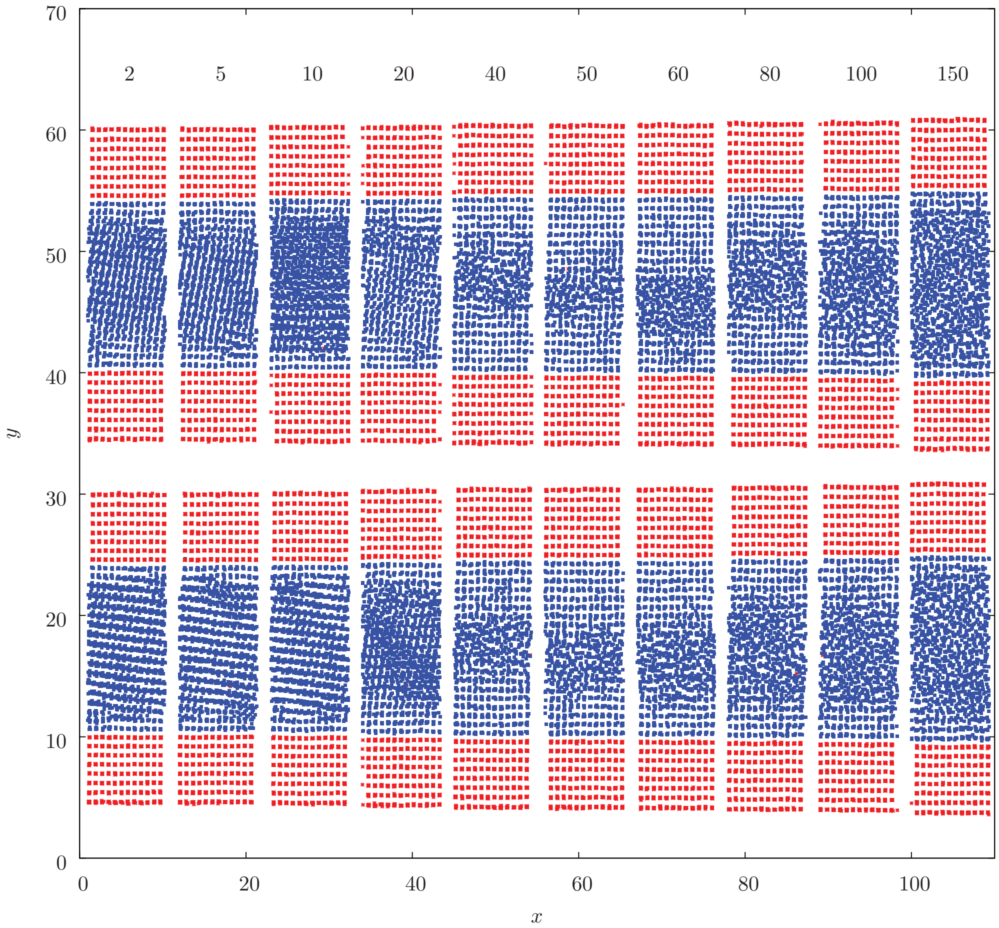

FIG. 3. As for Fig. 1 except the sliding speed dependence of the projections of the instantaneous particle coordinates on the *xy* plane are shown for a constant pressure of 1000 MPa. The wall speed is shown in the figure in m s^{-1}. The top row is for ascending wall speed, from left to right, and the bottom row is for descending wall speed from right to left. The annotated values on the axes do not have absolute significance, as they incorporate the horizontal and vertical shifting of the frames to form the tableau.

for the broadening of the shear localization region seen in experiments of Bair *et al.* and in these simulations in Fig. 3. There is no significant temperature jump at the walls (i.e., insignificant Kapitza thermal resistance). The largest fluctuations in temperature (as for the density and *x*-velocity profiles) occur at the boundary between the wall and confined liquid, reflecting the difference between the atomic force fields and equations of motion on either side of that boundary.

Figure 6 shows *xy* plane molecular snapshot projections for a larger system ($N = 4032$) at variable wall speed and $P = 1000$ MPa. This system has a stronger wall-confined atom attraction ($\epsilon_{ww} = 4$) than for the systems of Figs. 1–3. The PS-CL transition is also evident in the 1000 MPa system, occurring at 30 ± 10 m s^{-1} for $\epsilon_{ww} = 4$ and 2 but at 15 ± 5 m s^{-1} for $\epsilon_{ww} = 1$ (see Table I), in both the ascending and descending wall speed directions. This trend is possibly due to the yield stress at the wall being higher for larger ϵ_{ww}, which shifts the phase transitions systematically to higher wall speeds. The PS-CL transition occurs at higher wall speed with increasing pressure. For $\epsilon_{ww} = 4$ to 1, the PS-CL transition wall speed for 5000 MPa pressure decreases from ~100 to 30 m s^{-1}. If the pressure is too high for a given experimental liquid, these transitions may occur at too high a wall speed to be experimentally accessible.

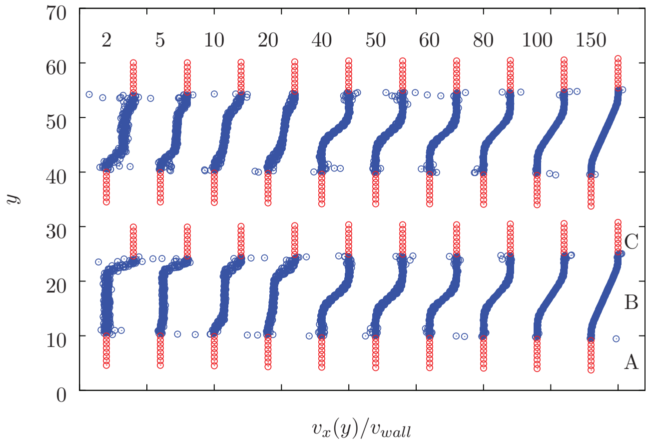

FIG. 4. The confined atom (blue online) and wall atom (red online) *x*-velocity profiles for the set of simulations of Fig. 2. The *S*2 set of parameters with a controlled normal pressure of 1000 MPa was used. The wall speeds are shown in the figure in m s^{-1}. The top row is for ascending wall speed (left to right), and the bottom row is for descending wall speed (right to left). The average velocity is normalized by the wall velocity. The annotated values on the axes are not absolute, as they incorporate horizontal and vertical shifting of the frames on the tableau.

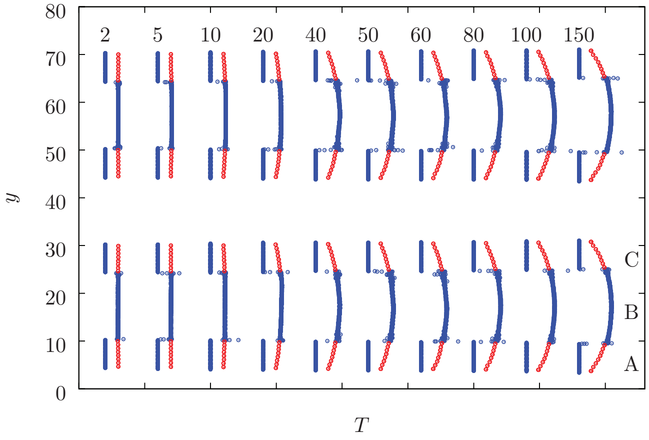

FIG. 5. The temperature profiles, T, based on the peculiar momenta kinetic energy. $T = 1$ is the target temperature in LJ units. The $S2$ set of input conditions from Table I was used. The wall speeds are shown in the figure in m s^{-1}. The top row is for ascending wall speed (v_x) left to right, and the bottom row is for descending wall speed, from right to left. The temperature of the wall atoms is shown (red online), averaged for each layer, as well separated symbols on either side of the confined atom region (blue online). The continuous vertical lines (blue online) in regions A and C indicate zero on the temperature scale for each frame. Again the numbers on the abscissa and ordinate include the horizontal and vertical shift increments, respectively. The abscissa tick marks correspond to 5σ intervals.

Non-wetting is associated with pronounced slip at the wall,[38] low energy dissipation, rapid fluid flow,[49] and large thermal slip lengths.[50] It is expected that the wetting parameter, c, in the wall-confined atom potential, should have a major effect on the structural states and shear localization produced in the NEMD simulations. Figure 7 presents zy plane molecule projection snapshots for a $N = 2592$ simulation using the wetting parameter in the interaction potential, $c = 0.1$ together with the parameter set S5 in Table I with an applied pressure of 1000 MPa. This causes essentially non-wetting of zone B atoms on those of A and C. This system exhibits a greater degree of slip at the wall, as observed previously by Barrat and Bocquet for non-wetting model liquids.[38] The two phase co-existence for this simulation occurs at a much higher wall speed than for the $c = 1$ case, and it took a somewhat different form with a solidlike phase adhering to one wall and a liquidlike phase persisting against the other wall. For increasing shear rate, the solid part of region B is commensurate with the upper wall, while for decreasing shear rate it adheres to the lower wall. The weaker degree of dynamical coupling between the wall and confined atoms also causes larger long-lived fluctuations and asymmetry in the local velocity profile. There is no statistical difference between the temperature on both sides of the wall boundary below the ordering transition, while above it there is a significant discontinuity in temperature at the wall. The region A and C temperature at the wall boundary is typically 25% lower than the region B temperature. The temperature profiles for very low wetting liquids

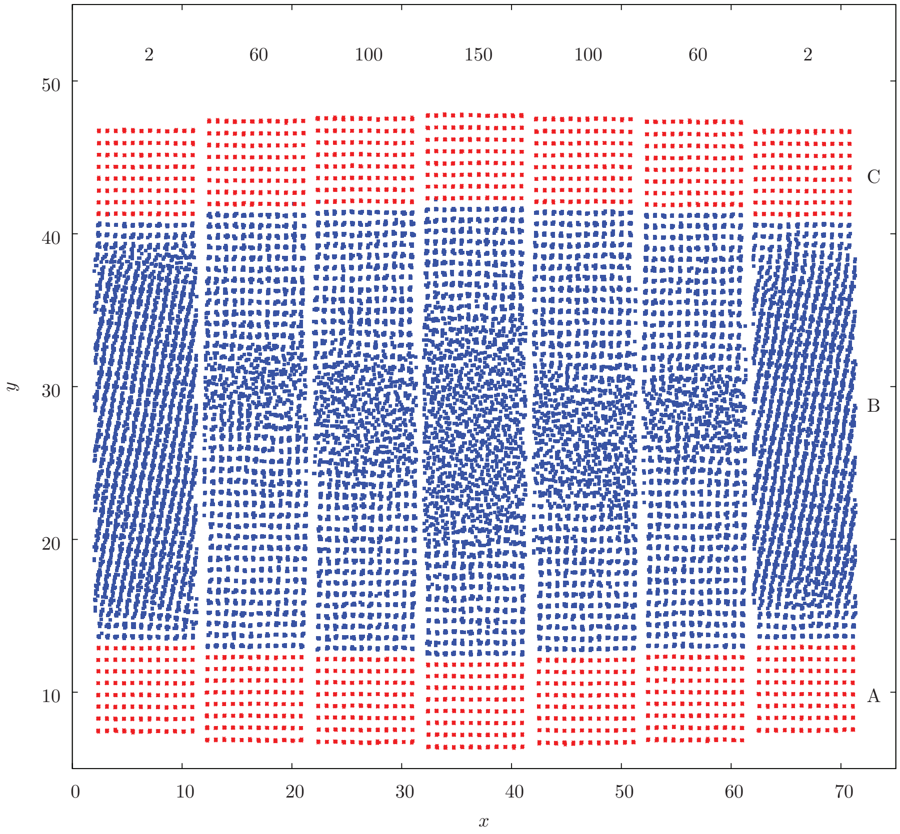

FIG. 6. The wall speed (in m s^{-1}) dependence of the xy projections of the particle coordinates for an applied pressure of 1000 MPa for $N = 4032$ atoms in total for the NEMD system. The $S1$ set of simulation parameters was used, with $\epsilon_w = 4$, and the Nosé-Hoover thermostat was applied to the outer two layers of the solid walls. The wall speeds are given in the figure in chronological order from left to right. The abscissa tick marks correspond to 5σ intervals.

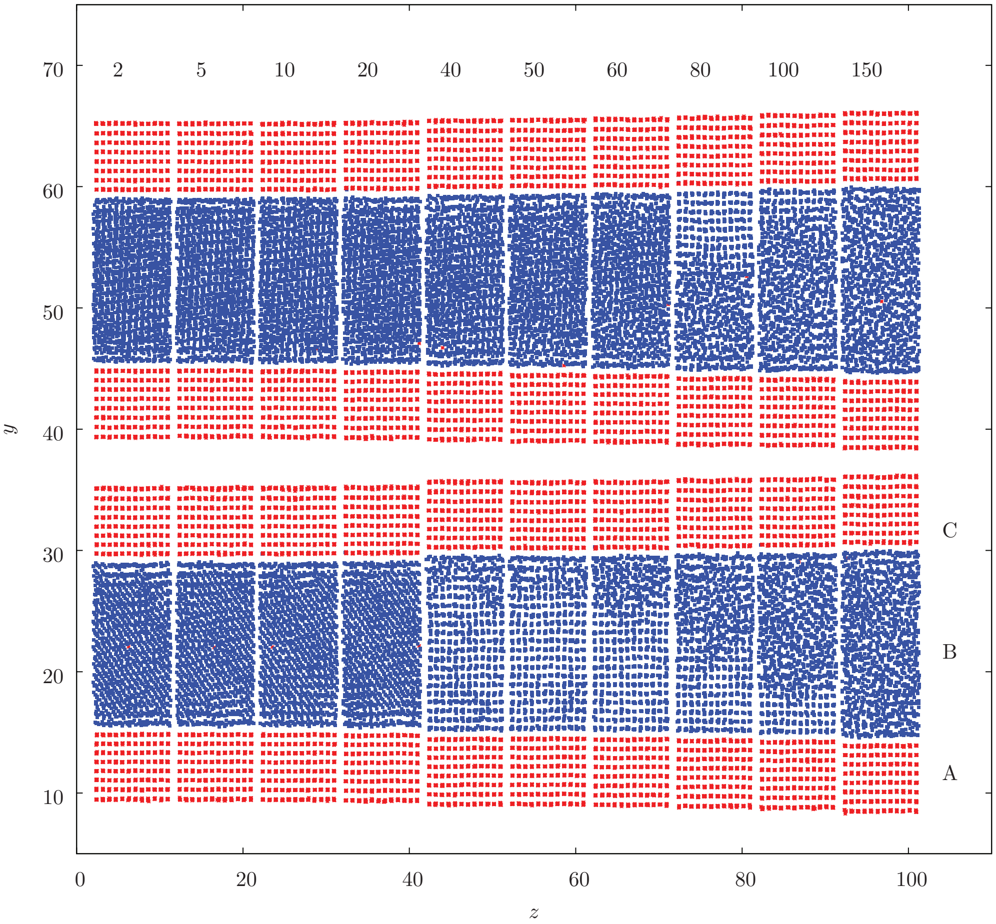

FIG. 7. The wall speed dependence of the *zy* projections of the instantaneous particle coordinates. The NEMD parameters are set S5 from Table I. The normal load was 1000 MPa, and the wetting parameter was equal to 0.1. The wall speed values given in the figure are in m s^{-1}. The numbers annotated on the axes are not absolute, as they incorporate the horizontal and vertical shifting of the frames required to form the frame sequence.

($c = 0.1$) therefore can show a major temperature decrease at the wall, as was discovered by Barrat and Chiaruttini,[50,51] and which is also evident in these simulations.

The stress tensor in these systems is considered now. In Ref. 52 a variable, $G(y)$, was defined as the y-integral of the sum of the pressure tensor at y and a y-dependent function of the external field. For the xy and yy components of the pressure tensor, $G(y)$, should on average be independent of y to comply with steady state mechanical equilibrium. Two formally equivalent routes can be used to compute $G(y)$ in the NEMD simulation, one based on averaging over a thin (i.e., $\Delta y \ll \sigma$) volume of infinite extent in the xz plane and centered at y, and the other from the molecules and forces which cross the xz plane at y. These two methods, called the volume averaging (VA) and the method of planes (MOP), respectively, are identical in the limit of infinitely thin bin thickness.[52] The equations and computational details required to compute $G(y)$ in the present slit pore geometry are given in Ref. 52. Figure 8 shows $G(y)$ for the $P_{xy}(y)$ and $P_{yy}(y)$ profiles at 1000 MPa with a wall speed of 40 m s^{-1} using the S2 parameter set of Table I, and during the increasing speed part of the simulation sequence. This is near the PS-CL transition. The $P_{xx}(y)$ and $P_{zz}(y)$ from VA are also shown as circles. The corresponding density and streamwise velocity profiles, and an instantaneous snapshot of the atom positions in the yx plane are also presented on this figure. The VA and MOP methods for P_{xy} and P_{yy} in the figure are constant and statistically indistinguishable on a sub-atomic length scale even under the extreme conditions of these simulations. The velocity profile extends part way into the solid region, and the diffuse density profile also reveals that the boundary between liquidlike and solid regions is not sharp, which is consistent with the results of Butler and Harrowell who showed from their NEMD simulations that the velocity field penetrates into the solid part at steady state for coexisting strained crystal and sheared liquid.[43] Shear banding or localization occurs here under homogeneous shear stress, and the variations in local shear rate in the system must, therefore, be attributable to local variations in its physical state in the y-direction. Figure 9 presents the same properties as in Fig. 8 but for a wall speed of 150 m s^{-1}. From the density and velocity profiles, it may be concluded that the confined region is clearly liquidlike throughout most of region B, with an almost linear velocity profile between the two walls, before leveling off within the ordered zone about three layers of confined molecules from each wall.

Turning now to the tribological aspects of these simulations, the traction coefficient, μ, the ratio of the shear to normal stress, is an important dimensionless quantity used to quantify the ability of a liquid to transmit shear force between

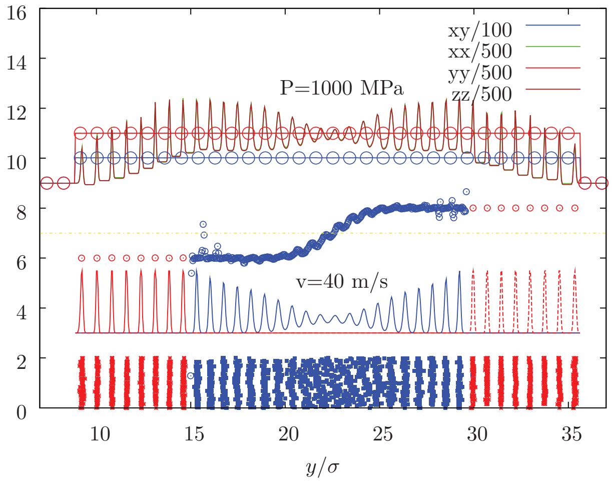

FIG. 8. A comparison between several y-dependent profiles. Regions $A-C$ follow from left to right. The applied pressure, $P = 1000$ MPa and $v_x = 40$ m s^{-1} for the $S2$ set of parameters. Top: The pressures tensor profiles, P_{xx}, P_{yy}, P_{zz}, and $-P_{xy}$. For the yy and xy cases the tethered wall correction was added in, so the total, referred to as $G(y)$ in Ref. 52, is plotted instead. Normalization factors for each quantity are indicated in the figure key. The normalized velocity profile, $v_x(y)$ for regions A/C (red symbols online) and B (blue online) are shown below the pressure tensor profiles. The normalized density profile, $\rho(y)$ for all three regions is given further below (red online for the wall regions and blue for the confined molecule region). A snapshot projection of the atom positions on the yx plane is shown in the bottom frame (y is horizontal and x is vertical in this case).

moving members in an engine. Liquids chosen to maximise μ are known as traction fluids, and these exhibit typical traction coefficient values of $\mu \simeq 0.12 - 0.14$.[53–55] The traction coefficient of the present model liquids was computed from the method of planes and volume average simulation values for the shear and normal stress. Figure 10 presents the traction coefficient curves as a function of wall speed using the S2 set of parameters at $P = 100$, 1000, and 5000 MPa (from left to right in the figure). At 100 MPa, the left-most frame in the figure, μ, increases monotonically and ultimately nonlinearly with sliding speed, reaching a value of 0.07 at the maximum wall speed of 150 m s^{-1} used. The upwards and downwards wall speed the μ are hardly different. The decreasing slope of this curve with increasing shear rate is indicative of shear thinning or softening of the confined material. These profiles are very similar to the traction curves of experimental lubricants, where maximum values of ∼0.07 are typical. A nonlinear dependence of the shear stress with shear rate of a sample in a confined geometry has been observed to vary as, $P_{xy} \sim \dot{\gamma}^m$ for a wide range of systems,[56] such as emulsions,[57] and soft particle pastes,[26] with values of m between 1/3 and 1/2 being typical. For the left frame of Fig. 10, the analytic form of $P_{xy}(\dot{\gamma}^m)$ is apparently not so simple as the effective exponent, m, decreases continuously with increasing $\dot{\gamma}$. Table II gives the maximum values of the traction coefficient, denoted by, μ_m, for the different parameter sets during the ascending and descending wall speed parts of the run sequence.

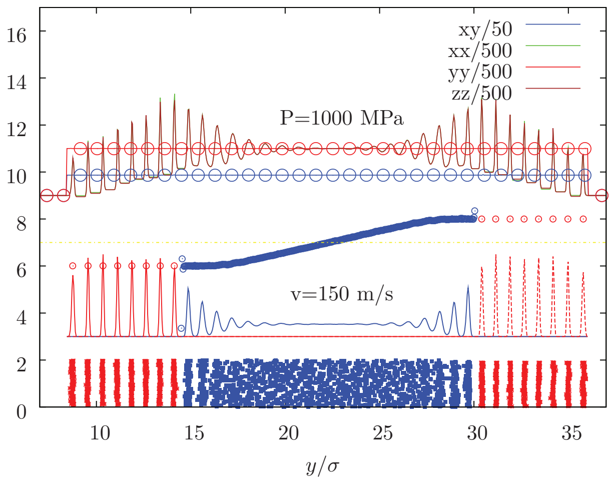

FIG. 9. As for Fig. 8 except the wall speed, $v_x = 150$ ms $^{-1}$.

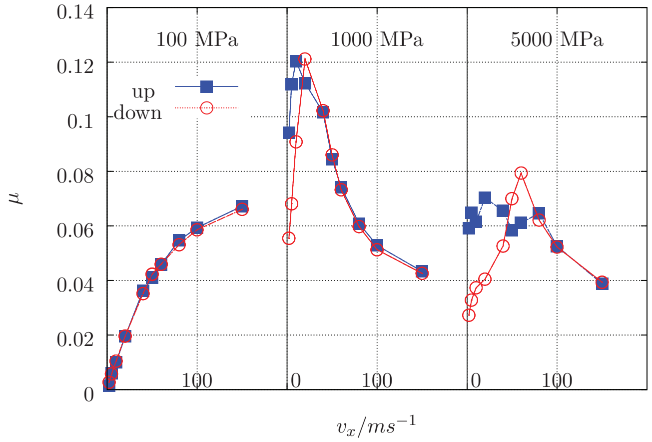

FIG. 10. The traction coefficient, μ, as a function of wall speed, v_x in m s^{-1}, for three applied pressure values, 100, 1000, and 5000 MPa (from left to right in the figure). The values for ascending v_x are represented by filled in squares and those descending, by open circles.

At 1000 MPa the traction coefficient against wall speed profile is quite different, showing a maximum of typically, 0.12 ± 0.01 during ascending and descending wall speed stages. Table II reveals that despite some statistical variation, the wall speed corresponding to the maximum traction coeffi-

TABLE II. Summary of the NEMD traction coefficient data. Key: # is the simulation parameter set code from Table I. $v_{x,\,1}$ is the wall speed (in m s^{-1}) at which the traction coefficient, $\mu = P_{xy}/P^0$, has its maximum value, on increasing v_x progressively in increments. The maximum in the traction coefficient over the ascending sliding speed range is denoted by, μ_m, which occurred at wall speed, $v_{x,\,1}$. The corresponding wall speed for maximum traction coefficient is $v_{x,\,2}$ on decreasing the wall speed. The values of P^0 in MPa are given in the second line of the column headings. The statistical uncertainties in μ are estimated to be ±0.005.

	$v_{x,\,1}$	μ_m	$v_{x,\,2}$	μ_m	$v_{x,\,1}$	μ_m	$v_{x,\,2}$	μ_m
#	1000	1000	1000	1000	5000	5000	5000	5000
S1	40	0.131	40	0.130	100	0.089	80	0.095
S2	10	0.120	20	0.121	20	0.073	60	0.079
S3	10	0.110	20	0.110	5	0.087	40	0.062
S4	40	0.132	40	0.135	20	0.104	100	0.102
S5	<2	0.149	40	0.092	60	0.067	80	0.059
S6	10	0.123	40	0.134	100	0.109	100	0.108
S7	10	0.120	40	0.105	60	0.075	60	0.078

cient is typically close to the PS-CL transition, and somewhat higher during descending wall speed. There is statistically significant hysteresis in the value of μ between the up and down v_x paths. For 5000 MPa, the upwards speed profile is rather flat, probably reflecting the strong slip at the walls until a wall speed of about 80 m s^{-1} is reached, above which the traction coefficient decreases with speed. Hysteresis is clearly evident at 5000 MPa, and there are large fluctuations in the traction coefficient between separate run sequences. The traction coefficient rarely exceeds a value of 0.07 at this pressure. The rather large maximum traction coefficient for $c = 0.1$ for a wall speed of about 1 m s^{-1} (set S5 in Table II) is a spike at the start of wall speed ascent and is presumably from an initial jammed state. A more representative value for the traction coefficient maximum on the way up in wall speed is 0.065, and 0.09 on the way down, both occurring at a wall speed of $\backsim$50 m s^{-1}. Therefore, maximum traction coefficients do not necessarily increase with pressure, and the applied pressure can be too high for optimum μ.

The yield stress of a single crystal is associated with the sliding of two adjacent planes at a critical applied shear stress of about 3% of the infinite frequency shear modulus, G_∞.[58,59] The shear elastic modulus of the LJ FCC solid at $T = 1$ was computed in a separate bulk solid MD calculation.[60,61] At 100, 1000, and 5000 MPa pressure, the computed shear modulus values were, 1798, 4549, and 14429 MPa, respectively. Figure 11 presents the ratio of the shear stress to infinite frequency shear modulus as a function of wall speed at the three applied pressures. The figure shows that the peak in μ for $P = 1000$ MPa occurs when the shear stress approximately exceeds a value between 2% $-$ 3% of the shear modulus, in agreement with theory.

The heat generated by the shearing process was extracted at the edge of the boundary walls (the outer two layers only were typically thermostatted, see Table I). At steady state, a temperature profile, $T(y)$, formed, with the maximum value at the center of the system. As the temperature profile is symmetric on average about the center of the film, it is convenient to reset the origin of the coordinate system to be at the center. A reasonable approximation is to represent the system in terms of three possible thermal states, a liquidlike region ("L") for $0 \le y \le y_1$, a crystallized part of region, B (S_1) for $y_1 \le y \le y_2$, and the tethered solid wall (S_2) for the distance range, $y_2 \le y \le y_3$ (i.e., region C). The boundary y-values between these three physical states can be located approximately from the x-velocity and density profiles for each simulation. The NEMD temperature profile, $T(y)$ can be compared with the prediction of Fourier's heat conduction law,[62]

$$\rho C \frac{\partial T}{\partial t} = \lambda \frac{\partial^2 T}{\partial y^2} + \dot{q}(y,t), \tag{5}$$

where C is the heat capacity at constant pressure, λ is the thermal conductivity, and $\dot{q}$ is the rate of heat production. For notational convenience and symmetry reasons, only the $y > 0$ half of the temperature profile is considered in the following analysis. At steady state the left-hand side of Eq. (5) is zero. Also, to a first approximation, it is assumed that $\dot{q} = 0$ in the solidlike regions of the system and there is a linear velocity profile in the liquidlike region of the confined film. The shear stress is defined in this context to be a positive quantity. The rate of heat production in the central liquidlike phase is approximated by, $\eta\dot{\gamma}^2 = P_{xy}\dot{\gamma}$,[63] where $\dot{\gamma} = v_x/y_1$. The viscosity is not calculated separately as P_{xy} is constant across the sample in the y direction at steady state (see Figs. 8 and 11), so any y-dependent effective viscosity can be estimated directly from the velocity gradient at that point. The heat flux ($-\lambda dT/dy$) is zero across the center line at $y = 0$ by symmetry because the temperature gradient is zero there. Consequently,

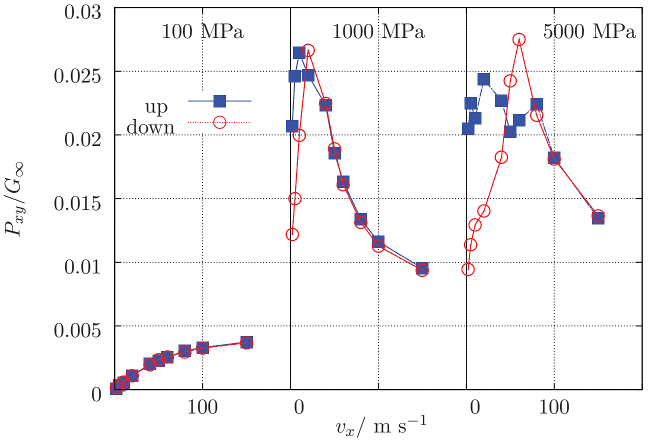

FIG. 11. The ratio of the shear stress to the shear rigidity modulus, P_{xy}/G_∞, is shown as a function of wall speed, v_x in m s^{-1}, for three applied pressure values given in the figure. The shear stress is defined as a positive quantity here. The values for ascending v_x are represented by filled in squares and those for descending speed by open circles.

$$\begin{aligned} T_L(y) &= -\frac{P_{xy}\dot{\gamma} y^2}{2\lambda_L} + A, \quad 0 \le y \le y_1, \\ T_{S1}(y) &= B_1 y + C_1, \quad y_1 \le y \le y_2, \\ T_{S2}(y) &= B_2 y + C_2, \quad y_2 \le y \le y_3. \end{aligned} \tag{6}$$

The five unknowns, A, B_1, C_1, B_2, C_2, can be obtained by equating the temperature and heat flux of two adjacent phases at the two boundaries at y_1 and y_2, and from $T_{S2}(y_3) = T_0$, the target outer boundary temperature. Let λ_L, λ_{S1}, and λ_{S2}, be the thermal conductivity of the central liquidlike region, and solid regions 1 and 2, respectively. The solution of Eq. (6) is

$$\begin{aligned} B_1 &= -\frac{P_{xy}\dot{\gamma}}{\lambda_{S1}} y_1, \\ B_2 &= \frac{\lambda_{S1}}{\lambda_{S2}} B_1, \\ C_2 &= T_0 - B_2 y_3, \\ C_1 &= (B_2 - B_1) y_2 + C_2, \\ A &= \frac{P_{xy}\dot{\gamma}}{2\lambda_L} y_1^2 + B_1 y_1 + C_1. \end{aligned} \tag{7}$$

Figure. 12 shows three temperature profiles, $T(y)$, determined directly from NEMD simulations at a wall speed of 150 m s^{-1} and from the above theory based on Fourier's law. The parameters in Eq. (7) were obtained by a least squares fit to the set of equations in Eq. (6) treating the three thermal conductivities as adjustable parameters. The maximum temper-

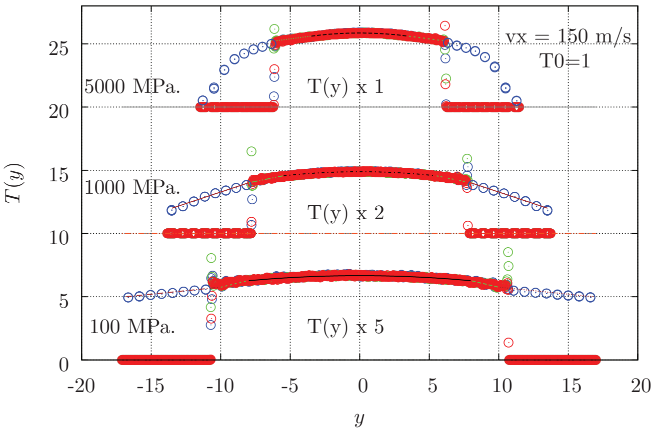

FIG. 12. Temperature profiles, $T(y)$, for the wall sliding speed of 150 m s^{-1} and $P = 100$, 1000, and 5000 MPa, from bottom to top. Note that the three curves are scaled differently in the figure to highlight the shape of the temperature profile in each case. The symbols are the MD simulation data, with the separated symbols on either side of the figure being for the tethered wall atoms (blue online). The continuous lines are the analytic solution from Eqs. (6) and (7). The values of the thermal conductivity are given in the main text. For $P = 100$ MPa, y_1, y_2 = 8.0, 10.0, and y_3 = 16.8 in σ; for $P = 1000$ MPa, y_1, y_2, and y_3 are, 5.5, 8.0, and 13.5, respectively; and these quantities are, 3.5, 6.0, and 11.4, for $P = 5000$ MPa. The shear stress values (P_{xy}) for the three pressures were 6.7, 43.4, and 194 in reduced units, respectively. The least square fit values for λ_{S1} are 2.95, 8.8, and 31 for $P = 100$, 1000, and 5000 MPa, respectively. For λ_L these are, 7.6, 16.9, and 31, and for λ_{S2} the values are 6.9 and 5.4 for $P = 100$ and 1000, respectively.

ature in the central region of the confined sample was 1.34, 2.43, and 5.9 for pressures of 100, 1000, and 5000 MPa (bottom to top frames, respectively). The thermal conductivity of the solid state at the various pressures considered was calculated independently from equilibrium MD simulations using a Green-Kubo time-correlation function formula.[64,65] At 100, 1000, and 5000 MPa, which corresponds to a bulk LJ reduced density in the solid phase of 1.027, 1.22, and 1.54, respectively, the thermal conductivity λ_{S1}, given by an equilibrium simulation was 17.5, 39.0, and 303 in reduced units. However, solids S_1 and S_2 are not "normal" solids, in that S_2 is tethered and the S_1 atoms are in registry with the tethered wall atoms, and at a lower density than predicted from the Lennard-Jones bulk equation of state at the given pressure. The simulation-fitted thermal conductivity values given in the figure caption are, therefore, lower than the Green-Kubo values, as would be expected from their lower than normal densities. Fourier's law applies quite well for the two lower pressures in Fig. 12, but departures are evident at the extreme pressure of 5000 MPa, notably in the tethered wall region where the temperature profile is not linear but continues the curvature developed in region *B*. It is notable that the NEMD temperature profiles exhibit a gradual smooth variation throughout the whole system in the y-direction and across the various boundaries, possibly due to dislocation-generated heat in the solid components and the imposed thermostatting constraints whose effects are not included in Eqs. (6) and (7). The wall and confined atoms should, therefore, be considered to be a single dynamical system in which the various parts are strongly coupled. From the shear stress and the local shear rate in the central liquidlike region, the effective shear viscosity, η has the values 1.4, 6.0, and 17, for $P = 100$, 1000, and 5000 MPa, respectively.

Bair *et al.*[31] considered the effect of thermal heating on tribology in terms of the Brinkman number, B_c, which measures the tendency of the liquid film to remain isothermal during boundary-driven shearing. In practice the film can be considered to be negligibly heated and isothermal if $B_c \ll 1$. The definition of B_c is

$$B_c = \frac{\beta P_{xy}^2 h^2}{\lambda_L \eta}, \tag{8}$$

where h is the film thickness, β is the temperature-viscosity coefficient, $\beta = -(\partial\eta/\partial T)/\eta$, and η is the bulk shear viscosity. For the LJ fluid, $h \simeq 2y_2$, $\eta \simeq 12\rho^4/T^{1/3}$,[5,66] where an effective density, $\rho = N_e/2S_x^2 y_2$ can be used. Taking (in reduced units) $T = 1$, $y_2 = 10.0$, 8.0, and 6.0, $P_{xy} = 0.16$, 1.03, and 4.61, and $\lambda_L = 7.6$, 16.9, and 31.0 for applied pressure, 100, 1000, and 5000, MPa, respectively, then $B_c = 0.08$, 0.39, and 0.76. The calculated Brinkman numbers are consistent with the NEMD temperature profiles, in that for 100 MPa, heating effects as indicated by the mid-plane height of $T(y)$ relative to the target wall temperature are predicted according to the Brinkman number to be rather modest, but relatively large at 5000 MPa.

Shear flow affects the phase diagram of a bulk system,[66–68] and it is therefore a natural extension to explore the non-equilibrium phase diagram of a confined liquid subject to boundary-driven shear flow. A schematic of the non-equilibrium phase diagram based on the present NEMD sim-

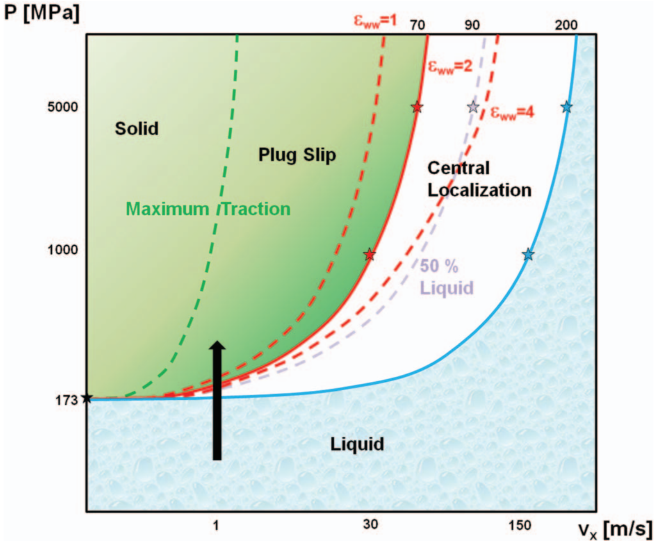

FIG. 13. Schematic non-equilibrium phase diagram for confined liquid boundary-driven shear flow, which shows the out-of-equilibrium phases as a function of applied load (P in MPa) and wall speed, v_x in m s^{-1} mainly for the S2 set of NEMD parameters. The domains of the phases discussed in the main text are shown in the figure. These are (non-slip) solid, liquid, plug slip (PS) and central localization (CL). The lever rule can be applied reasonably well to determine the percentage of the liquid phase in the CL region. The maximum traction is found typically in the PS region, close to its boundary with the CL phase. The depth of shading (green online) indicates the estimated relative magnitude of the maximum traction coefficient. The ϵ_{ww} lines (red online) indicate the approximate $PS - CL$ transition boundary line for values of this parameter. The stars indicate simulations performed, and the thick vertical arrow represents the transition in the confined liquid under pressure from a liquid to a solid state, corresponding to the simulations presented in Fig. 1.

ulations is shown in Fig. 13, projected on to the pressure *vs.* wall speed plane. The phases produced by the NEMD were reproducible and independent of simulation state point path history. The scale is for the molecularly thin Lennard-Jones fluids considered here, although it might be applicable to other types of liquid under comparable or corresponding states conditions. The diagram shows that the liquid region extends to higher pressure with increasing shear rate. The $v_x = 0$ line features the equilibrium solid-liquid phase co-existence boundary at $T^* = 1$.[46] Starting from low sliding speeds, the equilibrium solid phase deforms under shear through a dislocation mechanism (as discussed in the text in relation to Figs. 1 and 2). Above a critical shear rate, the yield stress at the wall is exceeded, and the system accommodates the global shear rate by slipping at the wall, while the central region forms a largely stationary but strained plug (the PS state). The next transition, at higher wall speed, involves shear localization in the center of the film, while the atoms near the boundaries crystallize into a solid phase commensurate with the wall atoms (the CL state). The proportion of the liquidlike central region increases with shear rate until it eventually fills the entire gap between the walls, joining up with the equilibrium fluid liquid region extended into nonequilibrium states and above another critical shear rate (wall speed). The wall slip part of the phase diagram will presumably be promoted by atomistically flat attractive walls. As given in Table I, the critical wall speed for the PS-CL transition increases with the wall-confined molecule attraction parameter, ϵ_{ww}, possibly because the yield stress at the boundary also increases with this parameter.

The central shear band thickness in the central localization phase broadens with increasing wall speed, as does the temperature of the confined region, which may therefore be the origin of the increasing width of the liquid-like region with shear rate (wall speed). There are, therefore, some common features with the adiabatic localization transition discovered by Bair *et al.*,[30,31,69] even though the experimental film thickness is typically $\sim 50 - 200$ μm, which corresponds to several thousand lubricant molecules across the gap, whereas between the walls in this NEMD study there were only $20-40$ spanning molecules. Also, as periodic boundaries operated in the streamwise and spanwise directions in the NEMD, it is perhaps not surprising that the banding observed in the simulation is parallel to the walls, rather than inclined at an angle as seen in the experiments.

IV. CONCLUSIONS

This work builds on the foundations of many previous NEMD studies of boundary-driven shear flow, in proposing a tentative generic phase diagram for continuously sheared confined liquids under pressure. Although it is perhaps stating the obvious, the presence of a wall-liquid boundary does have a major influence on the form of this non-equilibrium phase diagram under shear which distinguishes it from any comparable *bulk* phase diagram for the same chemical system. The boundary promotes shear localization, even for LJ liquids, which would not be observed under bulk shear conditions for this liquid, in contrast to the situation for thixotropic complex colloidal liquids which also shear band in the bulk.[26] The reason why the shear velocity gradient can localize in different parts of a slit channel as the applied shear rate changes is still not fully understood at a fundamental statistical mechanical level (as with many non-equilibrium phenomena). One important aspect of these systems is that at steady state the local shear stress from wall to wall, and within the walls, is constant on the atomic scale (see Figs. 8 and 9). With increasing shear stress, localization occurs first near the walls ("slip") where the confined molecules are ordered into layers, which form the natural support for material yielding by sliding. This is the region in the gap where the confined liquid has its lowest yield stress value. At higher stresses or global shear rates there appears from the present results to be an advantage in the system shearing away from the walls, as has in fact been observed experimentally (and discussed herein). At a particular global shear rate, the shear stress exceeds the yield stress of the material near the middle of the channel, and the system elects to shear-band away from the wall, allowing the rest of the confined liquid to reduce its potential energy by crystallizing or otherwise ordering against the wall and thereby gaining mechanical strength. The importance of such a transformation, indeed whether it will occur at all, will depend on the chemical compatibility and atomic-scale structural detail of the wall at the wall-liquid interface.

It is shown that understanding the tribology of molecularly thin films is in part equivalent to knowing the non-equilibrium phase diagram of the confined material in this geometry, as the two are intimately related, indeed are two sides of the same coin. It is shown here that the observed tribology, expressed in terms of the traction coefficient, μ, closely reflects these states of assembly and flow. The shear rates used in the present simulations are $10^8 - 10^{11}$ s^{-1}, which almost overlap with those which can be created in some tribological experiments $\sim 10^8$ s^{-1}. It is therefore not unreasonable to expect that some degree of rheological corresponding states could be used to project the present NEMD model results on to experimental system tribology at lower sliding speeds, as lubricant molecule relaxation times are much longer than those of argon (e.g., using a Peclet number type of treatment). This strategy has been applied to the bulk rheology of simple liquids computed by NEMD.[36,37] Despite using the simple Lennard-Jones potential, the simulations reproduce much of the tribology (some aspects quantitatively) of real lubricants in traction drives. It is often stated that the molecular architecture must be varied to give rise to optimum behavior through a "mechanism" with words like "interlocking" of molecules being used. Molecular simulation and experimental studies, e.g., Refs. 70 and 71 on traction fluids have given evidence for alignment or ordering of the molecules for those liquids that give the highest traction coefficients. The present simulations support these observations, as the confined liquid becomes ordered and solidlike under certain pressure and wall slip conditions which also give the highest traction coefficient values. In addition, *inter alia* these NEMD results suggest that the effect is more ubiquitous and not confined to certain "special" types of molecule. The fact that the basic monatomic

Lennard-Jones fluid shows the desired behavior suggests that the tribological trends observed are largely nonequilibrium "thermodynamic" in origin, and generic to most liquids for pressure and wall speeds whose range varies with molecular architecture. The lubricant molecules used in experimental traction applications are just those which happen to manifest these optimum trends (e.g., high traction coefficient) under the prevailing pressure, wall speed, and timescale conditions.

The accumulated evidence is that a transient phase transition from a liquid to solid state in the elasto-hydrodynamic lubrication contact may, therefore, give rise to the highest traction coefficient values. Soft-sphere scaling suggests why relatively compact molecules are most likely to cross the liquid-solid boundary line at a given temperature under pressure and hence give a high value for the traction coefficient. The fluid-solid coexistence pressure of the soft-sphere fluid scales as $P_{coex} \propto T^{1+3/n}$, where n is the potential exponent (i.e., $\phi(r) = 1/r^n$); so for the hard-sphere ($n \to \infty$) the coexistence pressure along the liquid-solid boundary on a P *vs.* T plot is linear with temperature, whereas for $n = 12$, $P_{coex} \propto T^{5/4}$, which is curving upwards and away from the liquidus line. Therefore small molecules, which have large n, have a greater probability of transforming from liquid to solid under pressure in the timescale of the lubricant being in the EHL contact zone. One might also expect small quite spherical molecules to have the shortest crystal nucleation times, which would also facilitate transient crystallization in the EHL contact zone. The form taken by the non-equilibrium phase diagram will depend on the system parameter set used. For example, for less attractive and atomistically rougher walls, the plug-slip region on the phase diagram may diminish in importance to an extent that there is a transformation directly from a solid without significant slip to a centrally sheared state.

On a technical level, for computational reasons the number of atoms that can be included in the NEMD simulation is many orders of magnitude smaller than present in any typical experimental system. The wall-liquid-wall sandwich NEMD model for channel flow carried out here should probably be viewed and treated as a single dynamical system, in which the three regions are strongly coupled in a structural and dynamical sense. This may partly explain, for example, the smooth temperature profile across the whole system observed in this study. Further investigation into optimum thermostatting strategies for NEMD boundary-driven flow would be beneficial.

ACKNOWLEDGMENT

D.M.H., H.A.S. and D.D. acknowledge the financial support received from the Engineering and Physical Sciences Research Council (EPSRC) UK via the Platform Grant EP/G026114/1. E.R.S thanks the Department of Mechanical Engineering at Imperial College London for the award of an EPSRC Doctoral Training Accounts scholarship.

[1] H. Docherty and P. T. Cummings, Soft Matter **6**, 1640 (2010).

[2] R. Pit, H. Hervet, and L. Léger, Phys. Rev. Lett. **85**, 980 (2000).

[3] H. Spikes and S. Granick, Langmuir **19**, 5065 (2003).

[4] E. Bonaccurso, M. Kappl, and H.-J. Butt, Phys. Rev. Lett. **88**, 076103 (2002).

[5] W. T. Ashurst and W. G. Hoover, Phys. Rev. A **11**, 658 (1975).

[6] S. Y. Liem, D. Brown, and J. H. R. Clarke, Phys. Rev. A **45**, 3706 (1992).

[7] J. Petravic and P. Harrowell, J. Chem. Phys. **124**, 014103 (2006).

[8] S. A. Gupta, H. D. Cochran, and P. T. Cummings, J. Chem. Phys. **107**, 10335 (1997).

[9] P. A. Thompson and M. O. Robbins, Phys. Rev. A **41**, 6830 (1990).

[10] A. Levent Demeril and S. Granick, J. Chem. Phys. **115**, 1498 (2001).

[11] M. Cieplak, J. Koplik, and J. R. Banavar, Phys. Rev. Lett. **86**, 803 (2001).

[12] P. A. Thompson and S. M. Troian, Nature (London) **389**, 360 (1997).

[13] N. V. Priezjev, Phys. Rev. E **75**, 051605 (2007).

[14] A. A. Pahlavan and J. B. Freund, Phys. Rev. E **83**, 021602 (2011).

[15] B. D. Todd, D. J. Evans, K. P. Travis, and P. J. Daivis, J. Chem. Phys. **111**, 10730 (1999).

[16] L. Zhu, C. Neto, and P. Attard, Langmuir **28**, 3465 (2012).

[17] E. Manias, G. Hadziioannou, I. Bitsanis, and G. ten Brinke, Europhys. Lett. **24**, 99 (1993).

[18] T. M. Galea and P. Attard, Langmuir **20**, 3477 (2004).

[19] A. V. Mokshin and J.-L. Barrat, Phys. Rev. E **77**, 021505 (2008).

[20] F. Varnik, L. Bocquet, J.-L. Barrat, and L. Berthier, Phys. Rev. Lett. **90**, 095702 (2003).

[21] D. Weiare, J. D. Barry, and S. Hutzler, J. Phys.: Condens. Matter **22**, 193101 (2010).

[22] P. Schall and M. van Hecke, Annu. Rev. Fluid Mech. **42**, 67 (2010).

[23] S. Bair and C. McCabe, Tribol. Int. **37**, 783 (2004).

[24] S. Manneville, A. Colin, G. Waton, and F. Schosseler, Phys. Rev. E **75**, 061502 (2007).

[25] P. C. F. Moller, J. Mewis, and D. Bonn, Soft Matter **2**, 274 (2006).

[26] S. P. Meeker, R. T. Bonnecaze, and M. Cloitre, Phys. Rev. Lett. **92**, 198302 (2004).

[27] Y. Zhang and A. L. Greer, Appl. Phys. Lett. **89**, 071907 (2006).

[28] J. S. Hansen, P. J. Daivis, K. P. Travis, and B. D. Todd, Phys. Rev. E **77**, 041121 (2007).

[29] R. M. Puscasu, B. D. Todd, P. J. Daivis, and J. S. Hansen, J. Phys.: Condens. Matter **22**, 195105 (2010).

[30] S. Bair, F. Qureshi, and W. O. Winer, ASME J. Tribol. **115**, 507 (1993).

[31] S. Bair, F. Qureshi, and M. Khonsara, ASME J. Tribol. **116**, 705 (1994).

[32] D. M. Heyes, J. Chem. Soc., Faraday Trans. 2 **82**, 1365 (1986).

[33] S. Butler and P. Harrowell, Nature (London) **415**, 1008 (2002).

[34] J. Ge, G.-W. Wu, B. D. Todd, and R. J. Sadus, J. Chem. Phys. **119**, 11017 (2003).

[35] L. Angelani, G. Ruocco, F. Sciortino, P. Tartaglia, and F. Zamponi, Phys. Rev. E **66**, 061505 (2002).

[36] D. M. Heyes, J. J. Kim, C. J. Montrose, and T. A. Litovitz, J. Chem. Phy. **73**, 3987 (1980).

[37] J. H. Simmons, R. K. Mohr, and C. J. Montrose, J. Appl. Phy. **53**, 4075 (1982).

[38] J.-L. Barrat and L. Bocquet, Phys Rev. Lett. **82**, 4671 (1999).

[39] S. Butler and P. Harrowell, J. Chem. Phys. **118**, 4115 (2003).

[40] M. P. Allen and D. J. Tildesley, *Computer Simulation of Liquids* (Oxford University Press, Oxford, 1987), p. 80.

[41] S. Bernardi, B. D. Todd, and D. J. Searles, J. Chem. Phys. **132**, 244706 (2010).

[42] R. Khare, J. de Pablo, and A. Yethiraj, J. Chem. Phys. **111**, 10732 (1999).

[43] S. Butler and P. Harrowell, Phys. Rev. E **67**, 051503 (2003).

[44] L. V. Woodcock, Chem. Phys. Lett. **10**, 257 (1971).

[45] T. Divoux, D. Tamarii, C. Barentin, and S. Mannevile, Phys. Rev. Lett. **104**, 208301 (2010).

[46] R. Agrawal and D. A. Kofke, Mol. Phys. **85**, 43 (1995).

[47] L. Isa, R. Besseling, and W. C. K. Poon, Phys Rev. Lett. **98**, 198305 (2007).

[48] N. Xu, C. S. O'Hern, and L. Kondic, Phys Rev. Lett. **94**, 016001 (2005).

[49] C. Liu and Z. Li, J. Chem. Phys. **132**, 24507 (2010).

[50] J.-L. Barrat and F. Chiaruttini, Mol. Phys. **101**, 1605 (2003).

[51] J. W. Lyver IV and E. Blaisten-Barojas, J. Phys.: Condens. Matter **21**, 345402 (2009).

[52] D. M. Heyes, E. R. Smith, D. Dini, and T. A. Zaki, J. Chem. Phys. **135**, 024512 (2011).

[53] S. H. Loewenthal and D. A. Rohn, NASA Technical Paper 2154, May 1983.

[54] S. Bair, *High-Pressure Rheology for Quantitive Elastohydrodynamics* (Elsevier, Oxford, 2007), p. 194.

[55] N. Fang, L. Chang, M. N. Webster, and A. Jackson, Tribol. Int. **33**, 751 (2000).

[56] H. Hu, G. A. Carson, and S. Granick, Phys. Rev. Lett. **66**, 2758 (1991).
[57] J. Goyon, A. Colin, G. Ovarlez, A. Ajdari, and L. Bocquet, Nature (London) **454**, 84 (2008).
[58] L.-B. Chen and C. F. Zukoski, J. Chem. Soc., Faraday Trans. **86**, 2629 (1990).
[59] D. Tabor, *Gases, Liquids and Solids*, 3rd ed. (Cambridge University Press, Cambridge, 1991), pp. 211–213.
[60] D. M. Heyes, J. Chem. Soc., Faraday Trans. 2 **85**, 239 (1989).
[61] D. M. Heyes and R. Szczepanski, J. Chem. Soc., Faraday Trans. 2 **83**, 319 (1987).
[62] B.-Y. Cao, J. Chem. Phys. **129**, 074106 (2008).
[63] J.-P. Ryckaert, A. Bellemans, G. Ciccotti, and G. V. Paolini, Phys Rev. Lett. **60**, 128 (1988).
[64] D. M. Heyes and J. G. Powles, Mol. Phys. **99**, 1077 (2001).
[65] K. V. Tretiakov and S. Scandolo, J. Chem. Phys. **120**, 3765 (2004).
[66] L. V. Woodcock, AIChE J. **52**, 438 (2006).
[67] L. V. Woodcock, Phys Rev. Lett. **54**, 1513 (1985).
[68] A. J. Hopkins, F. S. Jardali, and L. V. Woodcock, Mol. Simul. **4**, 241 (1989).
[69] S. Bair, Proc. Inst. Mech. Eng., Part J: J. Eng. Tribol. **223**, 617 (2009).
[70] H. Yamano, K. Shiota, R. Miura, M. Katagiri, M. Kubo, A. Stirling, E. Broclawik, A. Miyamoto, and T. Tsubouchi, Thin Solid Films **281**, 598 (1996).
[71] T. Tsubouchi and H. Hata, Tribol. Int. **28**, 335 (1995).
[72] W. Humphrey, A. Dalke and K. Schulten, J. Mol. Graphics **14**, 33 (1996).